

High-throughput screening for boride superconductors

Shiya Chen,¹ Zepeng Wu,¹ Zhen Zhang,² Shunqing Wu,¹ Kai-Ming Ho,² Vladimir Antropov,³ and Yang Sun¹

¹*Department of Physics, Xiamen University, Xiamen 361005, China*

²*Department of Physics, Iowa State University, Ames, Iowa 50011, USA*

³*Ames National Laboratory, Ames, Iowa 50011, USA*

A high-throughput screening using density functional calculations is performed to search for stable boride superconductors from the existing materials database. The workflow employs the fast frozen phonon method as the descriptor to evaluate the superconducting properties quickly. 23 stable candidates are identified from the screening. For almost all found binary compounds, the superconductivity was obtained earlier experimentally or computationally. For ternary borides, previous studies are very limited. Our extensive search among ternary systems confirmed superconductivity in known systems and found several new compounds. Among these discovered superconducting ternary borides, Ta(MoB)₂ shows the highest superconducting temperature of 12K. Most predicted compounds were synthesized previously; therefore, our predictions can be examined experimentally. Our work also demonstrates that the boride systems can have diverse structural motifs that lead to superconductivity.

I. INTRODUCTION

Superconducting materials have numerous applications in the modern society. The search for new superconductors with high critical superconducting temperature (T_c) is key to many future techniques in the energy, medical care, transportation, and quantum computing area. However, the conventional approaches to discovering new superconducting materials through direct experimental synthesis is time-consuming and resource-intensive. In recent years, it has been shown that computational prediction and design can greatly facilitate the discovery of new superconducting materials^{1,2}. The computational algorithms based on the density-functional perturbation theory (DFPT) can provide a satisfactory description of the electron-phonon coupling (EPC) and T_c for conventional superconductors. Due to the significant cost of the DFPT calculations, T_c calculations are now combined with information technologies such as data mining, machine learning, and high-throughput screening to guide the theoretical search of conventional superconductors³⁻⁶.

The discovery of superconductivity in the structurally simple MgB₂ compound^{6,7} has stimulated substantial research efforts toward uncovering phonon-mediated superconductors within similar chemistries. Many attempts have been made to identify new superconducting phases from the MgB₂ compound, such as chemical doping, which include Mg_{1-x}Li_xB₂⁸, Mg_{1-x}Zr_xB₂⁹. Some MgB₂-like boride systems, such as MoB₂¹⁰ and WB₂¹¹. Recently, we have shown that the Brillouin zone-centered EPC strength can be a simple descriptor to identify phonon-mediated superconducting materials in hydrides and borides¹²⁻¹⁷. This greatly reduced the computational cost in high-throughput screening of boride superconductors. While we identified a few novel boride systems that exhibit an interesting high T_c , its thermodynamic stability is not sufficiently high for synthesis and the structural motif is still very close to MgB₂. Therefore, it remains unclear if there are other stable struc-

tural motifs in the borides that can show feasible superconducting properties. In this study, we perform high-throughput screening on binary or ternary boride superconductors from existing materials database. These materials are stable and mostly synthesized before. We will use the zone-centered EPC strength as the main descriptor to identify their possible superconducting behavior. The structural motifs that can lead to possible T_c will be analyzed for the boride systems.

II. METHODS

Crystal structures are optimized by density functional theory calculations, which were performed using the projector augmented wave (PAW) method¹⁸ within density functional theory as implemented in the VASP code^{19,20}. The exchange and correlation energy is treated without the spin-polarized generalized gradient approximation (GGA) and parameterized by the Perdew-Burke-Ernzerhof formula (PBE)²¹. A plane-wave basis was used with a kinetic energy cutoff of 520 eV, and the convergence criterion for the total energy was set to 10^{-5} eV. Monkhorst-Pack's sampling scheme²² was adopted for Brillouin zone sampling with a k-point grid of $2\pi 0.033 \text{ \AA}^{-1}$. The lattice vectors (supercell shape and size) and atomic coordinates are fully relaxed until the force on each atom is less than 0.01 eV/Å. The initial screening of crystal structure were based on the MPRester package, which allows for the screening of materials from the Materials Project database²³. The high-throughput screening of strong EPC in these metal borides is based on the fast frozen-phonon calculation of the zone center EPC strength¹² defined by

$$\lambda_\Gamma = \sum_\nu \lambda_{\Gamma\nu}, \quad (1)$$

where Σ_ν indicates the summation of all modes at zone-center Γ_v is defined by

$$\lambda_{\Gamma v} = \frac{\tilde{\omega}_{\Gamma v}^2 - \omega_{\Gamma v}^2}{4\omega_{\Gamma v}^2}, \quad (2)$$

where $\tilde{\omega}_{\Gamma v}$ and $\omega_{\Gamma v}$ are unscreened and screened phonon frequencies of mode v at the zone-center, respectively. The screened phonon frequencies were calculated with the primitive cell and finite displacement methods implemented in the Phonopy code²⁴. The displacement amplitude in the frozen-phonon calculations is 0.02 Å. The convergence criterion of the total energy is 10-8 eV.

The calculations of full Brillouin-zone EPC constants and the superconducting temperature T_c of Be₂B, Ca₂Rh₅B₄, MoIrB₄ and TaMoB₂ were performed based on density functional perturbation theory (DFPT)²⁵ implemented in the Quantum ESPRESSO code^{19,26,27}. Ultrasoft pseudopotentials²⁸ with PBE functional were used with a kinetic energy cutoff of 80 Ry and a charge density cutoff of 800 Ry. After the convergence test, the plane-wave cutoff and the charge density cutoff were chosen to be 80 and 640 Ry, respectively. Monkhorst-Pack's sampling scheme²² was adopted for Brillouin-zone sampling with a k-point grid of $2\pi \times 0.025\text{Å}^{-1}$. Self-consistent field (SCF) calculations were performed with a dense k mesh of twice the scale of the sampling scheme, followed by the DFPT calculation with the k mesh of the same sampling scheme and set the q mesh to half of the k mesh. The isotropic Eliashberg spectral function was obtained via the average over the Brillouin zone^{29,30}

$$\alpha^2(\omega)F(\omega) = \frac{1}{2N(\epsilon_F)} \sum_{q\nu} \frac{\gamma_{q\nu}}{\hbar\omega q\nu} \delta(\omega - \omega_{q\nu}), \quad (3)$$

where $N(\epsilon_F)$ is the density of states at the Fermi level ϵ_F ; $\omega_{q\nu}$ denotes the phonon frequency of mode ν with wave vector q . $\gamma_{q\nu}$ is the phonon linewidth defined by

$$\gamma_{q\nu} = \frac{2\pi\omega_{q\nu}}{\Omega_{\text{BZ}}} \sum_{ij} \int d^3k \left| g_{k,q\nu}^{ij} \right|^2 \delta(\epsilon_{q,i} - \epsilon_F) \delta(\epsilon_{k+q,j} - \epsilon_F), \quad (4)$$

where $g_{k,q\nu}^{ij}$ is the EPC matrix element; $\epsilon_{q,i}$ and $\epsilon_{k+q,j}$ are eigenvalues of Kohn-Sham orbitals at bands i, j , and wave vectors q, k . The full Brillouin zone EPC constant λ is determined through the integration of the Eliashberg spectral function,

$$\gamma_{q\nu} = \frac{2\pi\omega_{q\nu}}{\lambda} = 2 \int \frac{\alpha^2(\omega)F(\omega)}{\omega} d\omega, \quad (5)$$

The T_c is obtained with the analytical McMillan formula²⁹ modified by Allen-Dynes (MAD)^{15,31}

$$T_c = \frac{\omega_{\log}}{1.2} \exp \left[\frac{-1.04(1 + \lambda)}{\lambda(1 - 0.62\mu^*) - \mu^*} \right], \quad (6)$$

where ω_{\log} is the logarithmic average frequency:

$$\omega_{\log} = \exp \left[\frac{2}{\lambda} \int \frac{d\omega}{\omega} \alpha^2(\omega)F(\omega) \ln \omega \right], \quad (7)$$

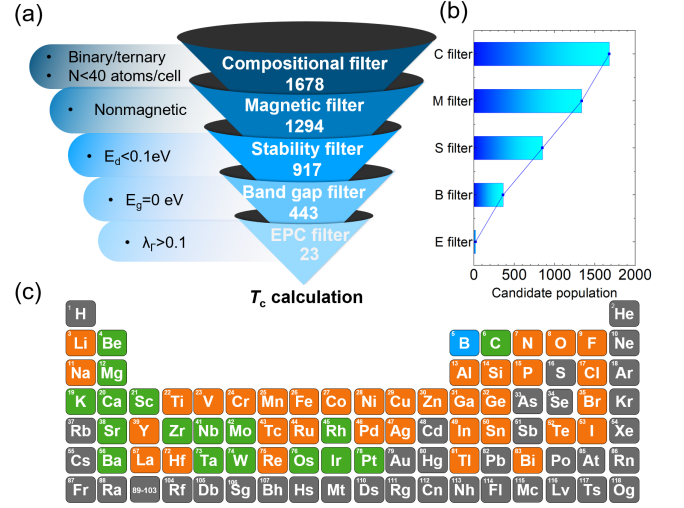


FIG. 1. (a) Schematics of screening workflow. (b) The bar chart of populations after each filter. (c) The elements involved in the screening. Orange indicates the elements in the initial pool after the B filter. Green indicates the remaining elements after the E filter.

and μ^* is the effectively screened Coulomb repulsion constant, set as 0.1 in our calculations.

III. RESULTS AND DISCUSSIONS

A. High throughput screening

Figure 1 summarizes the screening strategy for superconducting boride compounds²³. We design five criteria to filter low-energy binary or ternary borides for promising superconducting materials from the structure database³². These criteria include chemical composition filter (C), magnetic filter (M), stability filter (S), bands gap filter (B), and EPC strength filter (E). These filters are defined as follows.

The C-filter selects binary or ternary boride compounds containing fewer than 40 atoms in the primitive cell. These compounds contain various elements, as shown in Fig. 1(b). We eliminated compounds with rare-earth elements except for La due to the problematic DFT calculation for f electrons. The primary goal is to pinpoint simple binary or ternary borides for further consideration. This step effectively narrows down the candidate pool, resulting in 1678 phases for further evaluation.

The M-filter removes compounds with finite magnetic moment (larger than 0.01 $\mu\text{B}/\text{atom}$) from the pool, because the superconducting phases are mutually exclusive with the magnetic phase.

The S-filter attempts to select stable or low-energy metastable phases that exist in experiments or have a large chance of being synthesized. We employ the energy above the convex hull (E_d) less than 0.1 eV/atom as the

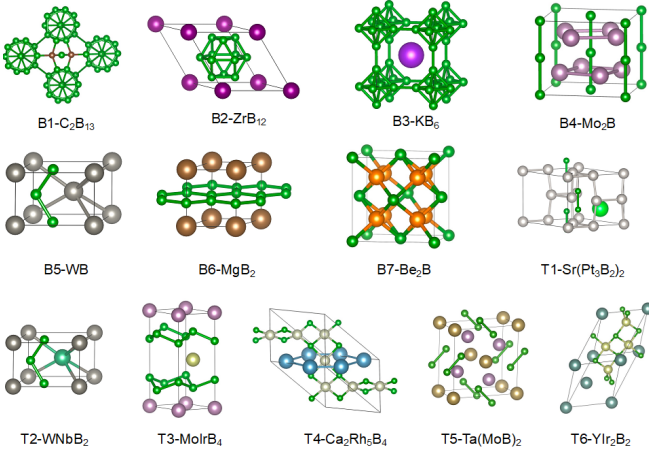


FIG. 2. Structural Motifs of potential superconducting boride phases.

criterion. measures the energy of a material to decompose into a set of stable materials. Larger E_d indicates poorer stability, while a zero E_d indicates this is the most stable phase. 0.1 eV/atom corresponds to the energy of thermal fluctuation 1100 K, a typical energy scale for the boride phase that can be synthesized experimentally¹⁵. The filter removed 377 unstable phases from the pool.

The B-filter selects metallic materials with zero band gap, a character commonly associated with superconductors. By implementing this filter, we eliminate semiconductors or insulators that are unlikely to exhibit superconducting behavior due to their electronic structure.

By applying these filtering and quantifying the number of materials at each step, we ensure the selected compounds align with our design principle for the potential superconductivity. Fig. 1 shows that the screening results in 443 candidates after B-filter. Before the final T_c calculations, we apply the E-filter to identify structures with strong EPC strength, which is based on the fast frozen-phonon calculations of zone-center EPC strength¹². This method is particularly efficient in identifying phonon-mediated superconductors in the borides and hydrides, where the zone-center phonon modes contributed significantly to the EPC^{13,15,16,33}. By setting a threshold of 0.1 for the zone-center EPC strength ($\lambda_r > 0.1$), we ultimately identified 23 materials for further superconductivity calculations. Comparing the candidate population after each filter in Fig. 1(b), it is evident that the EPC screening reduced the most significant fraction (95%) of the parent structure pool, suggesting strong EPC as a rare property in the materials.

The classified 23 candidates contain 12 binary compounds and 11 ternary compounds. As shown in Fig. 1(c), the elements involved in these compounds before E filter are evenly distributed in the elemental table and does not show a chemical preference. After applying the EPC filter, the remaining elements are mostly on the left side of the elemental table, showing a preference with

group-II elements. Based on the atomic packing, we classify the structures into 7 families for binary compounds and 6 families for ternary compounds. The structural information and motifs are shown in Table 1 and Fig. 2, respectively. The boron atoms exhibit diverse atomic packing in these motifs. In Motif B1, B2 and B3, boron atoms pack as B_{13} , B_{12} and B_6 polyhedra, respectively. In Motif B4 and B5, boron atoms pack as a chain. In Motif B6, boron forms a hexagonal layer. In Motif B7, boron forms a 3D structure with the metal atom. In ternary phases, boron's packing shows a similar motif as the ones in binary phases. In Motif T1, boron forms a dimmer structure. The Motif T2 is essentially the same as Motif B5 except that the metal site is occupied by different metal elements. Motif T3 is like B6, while the hexagonal boron layer is buckled. In Motif T4, boron and small metal atoms (Rh in the figure) form a square ring. The Motif T5 also has a B2 dimmer like T1. In Motif T6, each Ir atom is connected to four surrounding B atoms to form a ring, similar to the one in B7.

The screened superconducting phase shows diverse chemical and structural properties. In the following sections, we review relevant literature for synthesized superconductors in these structures. For structures that have not been explored, we will select a specific structure to conduct full Brillouin-zone EPC and T_c calculations. These will validate the reliability of our screening methodology and potentially discover new superconducting materials that have not been previously documented.

TABLE I. The structural and superconductivity properties of the screened candidate. Star (*) indicates the calculated result from this work. "Y" indicated the compound was previously synthesized.

Motif	Compound	λ_r	Syn?	Exp T_c	Cal T_c	Space group
B1	C_2B_{13}	0.36	Y ³⁴	-	15-30 K ³⁵	R-3m
B2	ZrB_{12}	0.14	Y ³⁶	6.0 K ³⁷	6.9 K*	Fm-3m
B3	KB_6	0.13	Y ³⁸	-	16.8 K ³⁹	Pm-3m
B4	Mo_2B	0.27	Y ⁴⁰	6.0 K ⁴¹	7.0 K*	I4/mcm
	Ta_2B	0.15	Y ⁴⁰	3 K ⁴²	-	
B5	WB	0.34	Y ⁴³	2.0 K ⁴⁴	5.3 K*	Cmcm
	MoB	0.32	Y ⁴³	2.4 K ⁴⁴	-	
B6	MgB_2	0.42	Y ⁴⁵	39 K ⁶	22 K ⁵¹	P6/mmm
	TaB_2	0.12	Y ⁴⁶	9 K ⁴⁹	1.5 K ⁵²	
	NbB_2	0.10	Y ⁴⁷	9 K ⁴⁴	5.7-19.4 K ⁵³	
	ScB_2	0.05	Y ⁴⁸	1 K ⁵⁰	<5 K ⁵⁰	
B7	Be_2B	0.34	Y ⁵⁴	-	10 K ⁵⁵	Fm-3m
T1	$Sr(Pt_3B_2)_2$	0.82	Y ⁵⁶	5 K ⁵⁷	4.1 K*	P-3m1
	$Ba(Pt_3B_2)_2$	0.64	Y ⁵⁶	5 K ⁵⁷	-	
T2	$WNbB_2$	0.22	Y ⁴⁷	-	2.4 K*	Amm2
	$TaMoB_2$	0.20	N	-	5 K*	
T3	$MoIrB_4$	0.10	N	-	4 K*	P-6m2
	$OsWB_4$	0.10	N	-	-	
T4	$Ca_2Rh_5B_4$	0.25	Y ⁵⁸	-	4.9 K*	Fmmm
	$Sr_2Rh_5B_4$	0.22	Y ⁵⁸	-	-	
T5	$Ta(MoB)_2$	0.93	Y ⁵⁹	-	12 K*	P4/mbm
	$Nb(MoB)_2$	0.57	Y ⁶⁰	-	-	
T6	YIr_2B_2	0.38	Y ⁶¹	3.3 K ⁶²	7.4 K	Fddd

B. Binary borides

Comparing with the literature, we find the majority of current binary candidates possess phonon-mediated superconductivity as shown in Table 1. Except MgB_2 , other compounds only show T_c lower than 10 K in the experimental study.

ZrB_{12} is a two-gap strongly coupled superconductor with experimental T_c of 6 K^{37,63}. In our calculation, T_c of ZrB_{12} was estimated 6.92 K by McMillan-Allen-Dynes (MAD) formula with $\lambda = 0.61$. and the low-frequency phonon modes dominated by the Zr atom contribute 0.34 to λ as shown in Fig. S11. Mo_2B was recently reported as a weakly coupled superconductor with T_c of 6 K⁴¹. However, there are some imaginary phonon modes at Γ point as shown in Fig. S12. It should be noted that the appearance of imaginary frequency modes in the phonon spectrum does not necessarily imply dynamical instability. Our calculations were based on the harmonic approximation, where the anharmonic effects and the quantum nuclear effect (QNE) were ignored. So, it was considered that when anharmonic effect was concluded, the system would be dynamically stable, such as CaSiO_3 ⁶⁴ SrTiO_3 ⁶⁵ Na_2TlSb ⁶⁶. Low T_c of 2 K in WB and MoB compounds were reported by Kayhan⁴⁴. There are some predicted superconductors, which are not demonstrated by experiment, such as KB_6 , C_2B_{13} , Be_2B . C_2B_{13} structure was predicted to be a potential superconductor with a T_c of 15-30 K³⁵. However, the experimentally synthesized C_2B_{13} contains a large number of defects, leading to a semiconducting state that hinders its superconductivity⁶⁷ KB_6 was calculated with T_c of 16.8 K³⁸. However, KB_6 has not yet to exhibit superconductivity in experiments. Possible factors include small, mutually insulated grains, inhibitory oxide impurities, adverse electronic localization, low magnetization experiment temperatures, and a disparity between theoretical predictions and practical superconductivity⁶⁸. Similarly, Be_2B was also predicted to be a potential superconductor⁶⁹ with T_c of 10 K⁵⁵. Unfortunately, the experimental synthesized Be_2B also contains defects and uncertainties on its stoichiometry⁷⁰.

C. Ternary borides

Table 1 shows several ternary borides as potential superconductor with $\lambda_F > 0.1$. Notably, among these ternary borides, the T1 family comprising $\text{Sr}(\text{Pt}_3\text{B}_2)_2$ and $\text{Ba}(\text{Pt}_3\text{B}_2)_2$ and T6 family (YIr_2B_2) were confirmed as superconductors by experiment⁵⁷. The EPC calculation results of $\text{Sr}(\text{Pt}_3\text{B}_2)_2$ and YIr_2B_2 were shown in Fig. S14 and Fig. S15. Similar to Mo_2B , $\text{Sr}(\text{Pt}_3\text{B}_2)_2$ was also harmonically unstable, where the anharmonic effect can be significant. Other ternary families have not been investigated for superconductivity by experiment or theory. We select one compound for each family in T2-T5 to perform DFPT calculations. The calculated full

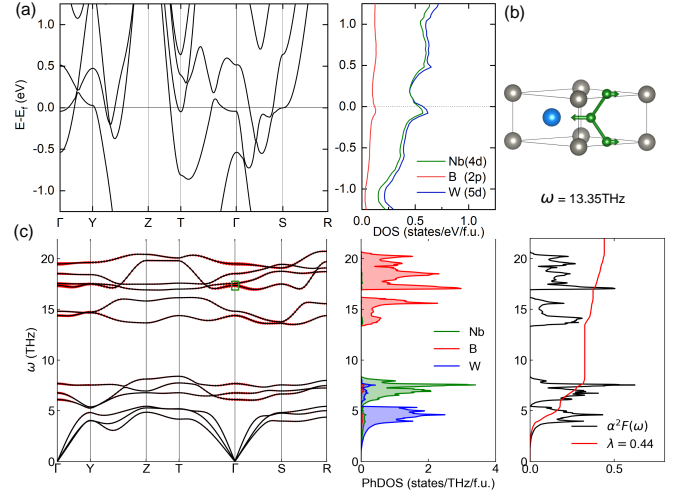


FIG. 3. (a) Band structure and projected density of states of WNbB_2 . (b) Structure of WNbB_2 . The arrow represents the eigenvector of phonon mode at the point with a frequency of 13.35 THz, noted in (c). Blue is W, gray is Nb and green is B. (c) Phonon spectrum, projected phonon density of state, and Eliashberg spectral function of WNbB_2 . The red bands on the phonon spectrum indicate the phonon linewidth.

Brillouin zone EPC constant and estimated T_c with the MAD formula are shown in Table 1 and discussed below.

WNbB₂. WNbB_2 shares the same crystal structure as WB. The B atoms in WNbB_2 exist in the form of a one-dimensional B atom chain see Fig. 3(b). As in Fig. 3(a), there is a van-Hove singularity near the Fermi level, mainly dominated by Nb-4d orbital and W-5d orbital. On the other hand, due to the significant mass differences between B and Nb/W, the phonon modes are entirely decoupled. Nb and W contribute to the EPC of low phonon frequency modes, while B contributes to the EPC of high phonon frequency modes. Fig. 3(b) shows the phonon mode with a frequency of 13.35 THz at Γ point, which possesses large phonon linewidth, contributing major EPC strength in high-frequency phonons.

The T_c of WNbB_2 is 2 K, smaller than WB (5.3K). The main reason for the difference in T_c between WNbB_2 and WB is that the λ contributed by low-frequency phonons in WB is higher than in WNbB_2 . Compared with WB, the introduction of the Nb element in WNbB_2 increases the frequency of some low-frequency optical phonons, suppresses the softening of phonons, and weakens EPC.

MoIrB₄. The band structure and phonon spectrum of MoIrB_4 are shown in Fig. 4. Projected electron density of states indicates that Ir-5d orbital dominates the $N(E_F)$, and Ir contributes significantly to EPC. The calculated T_c of MoIrB_4 is 4K. MoIrB_4 also exhibits layered structural characteristics. It shows some analogy to MgB_2 , in which the B atoms form interlayer hexagonal rings between metal layers. The distinction between MoIrB_4 and MgB_2 lies in that the B hexagonal rings in MoIrB_4 are not coplanar but rather adopt a buckled

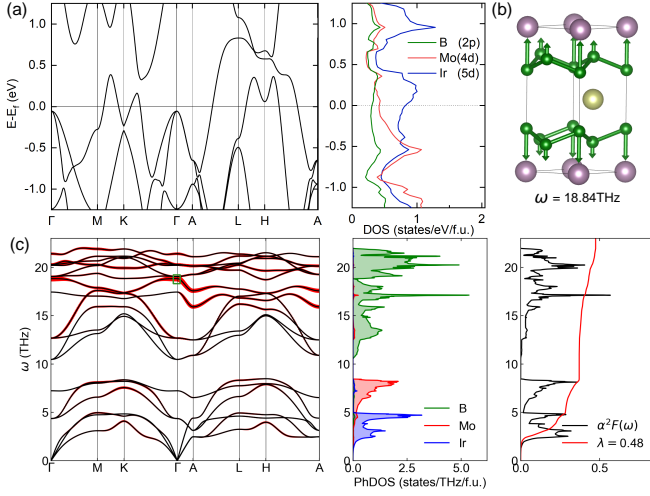


FIG. 4. (a) Band structure and projected density of states of MoIrB₄. (b) Structure of MoIrB₄. The arrow represents the eigenvector of phonon mode at point with frequency of 18.84 THz, noted in (c). Purple is Mo, yellow is Ir and green is B. (c) Phonon spectrum, projected phonon density of state and Eliashberg spectrum of MoIrB₄. The red bands on the phonon spectrum indicate the phonon linewidth.

three-dimensional conformation. This buckled structure may originate from the metal atoms above the B rings instead of at the ring centers, which compress the B rings and lead to corrugation deformation. The EPC strength in MgB₂ is mainly contributed by the in-plane vibration mode of B atoms⁷¹. However, the situation is different in MoIrB₄. The phonon mode with the largest linewidth among high-frequency phonons corresponds to the out-of-plane vibration of B atoms, as shown in Fig. 4(b).

Ca₂Rh₅B₄. Rh atom in Ca₂Rh₅B₄ is coplanar with the four surrounding B atoms with Rh-B bond length 2.16 Å, forming a series of RhB₄ units. These units are connected by sharing Rh atoms to form a framework. Ca atoms are embedded in this matrix framework. This structure was first synthesized in 1983⁵⁸. The band structure and phonon spectrum are shown in Fig. 5(a) and (c). Among B-dominated high-frequency phonons, the phonon mode with the largest phonon linewidth is the 26th mode at point (= 13.19 THz), which is the breathing vibration of B atoms in the RhB₄ cluster, shown in Fig. 5(b). The DFPT result indicates that Ca₂Rh₅B₄ is a potential superconductor with T_c = 4.9 K and λ = 0.72.

Ta(MoB)₂. The B2 dimmer in Ta(MoB)₂ has a B-B bond length of 1.89 Å. Although the contribution of B-dominated high-frequency phonon modes to EPC strength is weak, phonon mode dominated by heavy elements in the low-frequency region contributes to large EPC. T_c of Ta(MoB)₂ is 12 K and λ = 0.81. One of the modes that contributes significantly to EPC in the low-frequency region is the in-plane stretching vibration dominated by Mo atoms shown in Fig. 6(b). Phonon softening favors enhanced EPC, as observed in hydrides¹⁴. On

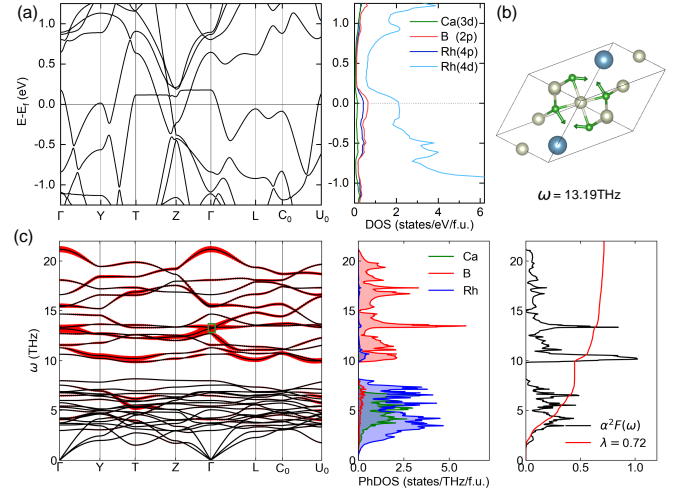


FIG. 5. (a) Band structure and projected density of states of Ca₂Rh₅B₄. (b) Structure of Ca₂Rh₅B₄. The arrow represents the eigenvector of phonon mode at point with frequency of 13.19 THz, noted in (c). Blue is Ca, yellow is Rh and green is B. (c) Phonon spectrum, projected phonon density of state, and Eliashberg spectrum of Ca₂Rh₅B₄. The red bands on the phonon spectrum indicate the strength of EPC.

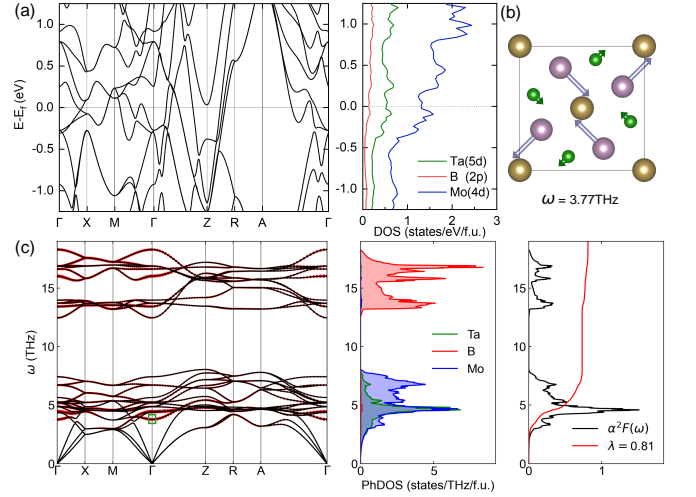


FIG. 6. (a) Band structure and projected density of states of Ta(MoB)₂. (b) Structure of Ta(MoB)₂. The arrow represents the eigenvector of phonon mode at point with frequency of 3.8 THz, noted in (c). Purple is Mo, yellow is Ta and green is B. (c) Phonon spectrum, projected phonon density of state, and Eliashberg spectral function of Ta(MoB)₂. The red bands on the phonon spectrum indicate the strength of EPC.

the other hand, high electron density of states is beneficial to strong EPC. The Van-Hove singularity below the Fermi level may regulate the E_f by hole doping or induce high-frequency phonon modes to soften by element doping. It is possible to improve further the superconducting temperature of Ta(MoB)₂.

IV. CONCLUSIONS

In summary, by applying a series of filters to extract binary and ternary boride candidates from the crystal structure database, we identified 23 promising candidates as potential superconductors. Further EPC calculations by DFPT revealed their EPC and superconducting temperature. While superconductivity in binary borides has been confirmed through experiments and computations, the superconductivity in ternary borides remains relatively unexplored. Notably, $\text{Ta}(\text{MoB})_2$ exhibits the highest superconducting temperature at approximately

12 K. Since most ternary compounds have been synthesized before, the predicted superconductivity can be validated through future experiments. This study highlights the potential of utilizing high-throughput computational screening to discover new superconducting materials. Additionally, it demonstrates that, apart from the well-studied MgB_2 structure, diverse structural motifs in borides can lead to superconductivity. These motifs could be the foundation for future high-throughput screening involving elemental substitution to discover new compounds.

-
- ¹ K. Choudhary and K. Garrity, Designing High-TC Superconductors with BCS-Inspired Screening, Density Functional Theory, and Deep-Learning, *npj Comput Mater* 8, 244 (2022).
 - ² J. A. Flores-Livas, L. Boeri, A. Sanna, G. Profeta, R. Arita, and M. Eremets, A Perspective on Conventional High-Temperature Superconductors at High Pressure: Methods and Materials, *Physics Reports* 856, 1 (2020).
 - ³ N. Hoffmann, T. F. T. Cerqueira, J. Schmidt, and M. A. L. Marques, Superconductivity in Antiperovskites, *npj Comput Mater* 8, 150 (2022).
 - ⁴ E. A. Pogue et al., Closed-Loop Superconducting Materials Discovery, *npj Comput Mater* 9, 181 (2023).
 - ⁵ T. F. T. Cerqueira, A. Sanna, and M. A. L. Marques, Sampling the Materials Space for Conventional Superconducting Compounds, *Advanced Materials* 36, 2307085 (2024).
 - ⁶ J. Nagamatsu, N. Nakagawa, T. Muranaka, Y. Zenitani, and J. Akimitsu, Superconductivity at 39 K in Magnesium Diboride, *Nature* 410, 6824 (2001).
 - ⁷ J. Kortus, I. I. Mazin, K. D. Belashchenko, V. P. Antropov, and L. L. Boyer, Superconductivity of Metallic Boron in MgB_2 , *Physical Review Letters* 86, 4656 (2001).
 - ⁸ I. Pallechi et al., Investigation of Li-Doped MgB_2 , *Supercond. Sci. Technol.* 22, 095014 (2009).
 - ⁹ Y. Feng, Y. Zhao, A. K. Pradhan, C. H. Cheng, J. K. F. Yau, L. Zhou, N. Koshizuka, and M. Murakami, Enhanced Flux Pinning in Zr-Doped MgB_2 Bulk Superconductors Prepared at Ambient Pressure, *Journal of Applied Physics* 92, 2614 (2002).
 - ¹⁰ C. Pei et al., Pressure-Induced Superconductivity at 32 K in MoB_2 , *National Science Review* 10, nwad034 (2023).
 - ¹¹ J. Lim et al., Creating Superconductivity in WB_2 through Pressure-Induced Metastable Planar Defects, *Nat Commun* 13, 7901 (2022).
 - ¹² Y. Sun, F. Zhang, C.-Z. Wang, K.-M. Ho, I. I. Mazin, and V. Antropov, Electron-Phonon Coupling Strength from Ab Initio Frozen-Phonon Approach, *Phys. Rev. Materials* 6, 074801 (2022).
 - ¹³ R. Wang, Y. Sun, F. Zhang, F. Zheng, Y. Fang, S. Wu, H. Dong, C.-Z. Wang, V. Antropov, and K.-M. Ho, High-Throughput Screening of Strong Electron-Phonon Couplings in Ternary Metal Diborides, *Inorg. Chem.* 61, 18154 (2022).
 - ¹⁴ Z. Wu, Y. Sun, A. P. Durajski, F. Zheng, V. Antropov, K.-M. Ho, and S. Wu, Effect of Doping on the Phase Stability and Superconductivity in LaH_{10} , *Phys. Rev. Mater.* 7, L101801 (2023).
 - ¹⁵ F. Zheng, Y. Sun, R. Wang, Y. Fang, F. Zhang, S. Wu, C.-Z. Wang, V. Antropov, and K.-M. Ho, Superconductivity in the Li-B-C System at 100 GPa, *Phys. Rev. B* 107, 014508 (2023).
 - ¹⁶ F. Zheng, Y. Sun, R. Wang, Y. Fang, F. Zhang, S. Wu, Q. Lin, C.-Z. Wang, V. Antropov, and K.-M. Ho, Prediction of Superconductivity in Metallic Boron-Carbon Compounds from 0 to 100 GPa by High-Throughput Screening, *Phys. Chem. Chem. Phys.* 25, 32594 (2023).
 - ¹⁷ Y. Sun, Z. Zhang, A. P. Porter, K. Kovnir, K.-M. Ho, and V. Antropov, Prediction of Van Hove Singularity Systems in Ternary Borides, *npj Comput Mater* 9, 204 (2023).
 - ¹⁸ P. E. Blöchl, Projector Augmented-Wave Method, *Phys. Rev. B* 50, 17953 (1994).
 - ¹⁹ G. Kresse and J. Furthmüller, Efficiency of Ab-Initio Total Energy Calculations for Metals and Semiconductors Using a Plane-Wave Basis Set, *Computational Materials Science* 6, 15 (1996).
 - ²⁰ G. Kresse and J. Furthmüller, Efficient Iterative Schemes for Ab Initio Total-Energy Calculations Using a Plane-Wave Basis Set, *Phys. Rev. B* 54, 11169 (1996).
 - ²¹ J. P. Perdew, K. Burke, and M. Ernzerhof, Generalized Gradient Approximation Made Simple, *Phys. Rev. Lett.* 77, 3865 (1996).
 - ²² H. J. Monkhorst and J. D. Pack, Special Points for Brillouin-Zone Integrations, *Phys. Rev. B* 13, 5188 (1976).
 - ²³ A. Jain et al., The Materials Project: A Materials Genome Approach to Accelerating Materials Innovation, *APL Materials* 1, 011002 (2013).
 - ²⁴ A. Togo and I. Tanaka, First Principles Phonon Calculations in Materials Science, *Scripta Materialia* 108, 1 (2015).
 - ²⁵ S. Baroni, S. de Gironcoli, A. Dal Corso, and P. Giannozzi, Phonons and Related Crystal Properties from Density-Functional Perturbation Theory, *Rev. Mod. Phys.* 73, 515 (2001).
 - ²⁶ P. Giannozzi et al., Advanced Capabilities for Materials Modelling with Quantum ESPRESSO, *J. Phys.: Condens. Matter* 29, 465901 (2017).
 - ²⁷ P. Giannozzi et al., Quantum ESPRESSO toward the Exascale, *The Journal of Chemical Physics* 152, 154105 (2020).
 - ²⁸ A. Dal Corso, Pseudopotentials Periodic Table: From H to Pu, *Comput. Mater. Sci.* 95, 337 (2014).

- ²⁹ W. L. McMillan, Transition Temperature of Strong-Coupled Superconductors, *Phys. Rev.* 167, 331 (1968).
- ³⁰ P. B. Allen and R. C. Dynes, Transition Temperature of Strong-Coupled Superconductors Reanalyzed, *Phys. Rev. B* 12, 905 (1975).
- ³¹ P. B. Allen, Neutron Spectroscopy of Superconductors, *Phys. Rev. B* 6, 2577 (1972).
- ³² A. Jain et al., The Materials Project: Accelerating Materials Design Through Theory-Driven Data and Tools, *APL Mater.* 1, 011002 (2013).
- ³³ Y. Sun, F. Zhang, S. Wu, V. Antropov, and K.-M. Ho, Effect of Nitrogen Doping and Pressure on the Stability LuH_3 , *Phys. Rev. B* 108, L020101 (2023).
- ³⁴ G. Will and K. H. Kossobutzki, An X-Ray Diffraction Analysis of Boron Carbide, B_{13}C_2 , *Journal of the Less Common Metals* 47, 43 (1976).
- ³⁵ M. Calandra, N. Vast, and F. Mauri, Superconductivity from Doping Boron Icosahedra, *Phys. Rev. B* 69, 224505 (2004).
- ³⁶ C. H. L. Kennard and L. Davis, Zirconium Dodecarborides ZrB_{12} . Confirmation of the B12 Cubooctahedral Unit, *Journal of Solid State Chemistry* 47, 103 (1983).
- ³⁷ Y. Wang, R. Lortz, Y. Paderno, V. Filippov, S. Abe, U. Tutsch, and A. Junod, Specific Heat and Magnetization of a ZrB_{12} Single Crystal: Characterization of a Type-II/1 Superconductor, *Phys. Rev. B* 72, 024548 (2005).
- ³⁸ A. Ammar et al., Investigation of the Electronic and Structural Properties of Potassium Hexaboride, KB_6 , by Transport, Magnetic Susceptibility, EPR, and NMR Measurements, Temperature-Dependent Crystal Structure Determination, and Electronic Band Structure Calculations, *Inorg. Chem.* 43, 4974 (2004).
- ³⁹ T. F. T. Cerqueira, A. Sanna, and M. A. L. Marques, Sampling the Materials Space for Conventional Superconducting Materials, *Adv. Mater.* 36, 2307085 (2024).
- ⁴⁰ E. E. Havinga, H. Damsma, and P. Hokkelling, Compounds and Pseudo-Binary Alloys with the $\text{CuAl}_2(\text{C16})$ -Type Structure I. Preparation and X-Ray Results, *Journal of the Less Common Metals* 27, 169 (1972).
- ⁴¹ Y. Ge, K. Bao, T. Ma, J. Zhang, C. Zhou, S. Ma, Q. Tao, P. Zhu, and T. Cui, Revealing the Unusual Boron-Pinned Layered Substructure in Superconducting Hard Molybdenum Semiboride, *ACS Omega* 6, 21436 (2021).
- ⁴² G. F. Hardy and J. K. Hulm, The Superconductivity of Some Transition Metal Compounds, *Phys. Rev.* 93, 1004 (1954).
- ⁴³ H. Haschke, H. Nowotny, and F. Benesovsky, Untersuchungen in den Dreistoffen: Mo, W-Fe, Co, Ni-B, *Monatshefte für Chemie* 97, 1459 (1966).
- ⁴⁴ M. Kayhan, Transition Metal Borides: Synthesis, Characterization and Superconducting Properties, Ph.D. Thesis, Technische Universität (2013).
- ⁴⁵ M. E. Jones and R. E. Marsh, The Preparation and Structure of Magnesium Boride, MgB_2 , *J. Am. Chem. Soc.* 76, 1434 (1954).
- ⁴⁶ J. T. Norton, H. Blumenthal, and S. J. Sindeband, Structure of Diborides of Titanium, Zirconium, Columbium, Tantalum and Vanadium, *JOM* 1, 749 (1949).
- ⁴⁷ Yu. B. Kuz'ma, V. I. Lakh, B. I. Stadnyk, and Yu. V. Voroshikov, X-Ray Diffraction Study of the System Niobium-Tungsten-Boron, *Powder Metall Met Ceram* 5, 491 (1966).
- ⁴⁸ A. Waśkowska, L. Gerward, J. Staun Olsen, K. Ramesh Babu, G. Vaitheeswaran, V. Kanchana, A. Svane, V. B. Filipov, G. Levchenko, and A. Lyaschenko, Thermoelastic Properties of ScB_2 , TiB_2 , YB_4 and HoB_4 : Experimental and Theoretical Studies, *Acta Materialia* 59, 4886 (2011).
- ⁴⁹ D. Kaczorowski, A. J. Zaleski, O. J. Żogał, and J. Klamut, Incipient Superconductivity in TaB_2 , *arXiv:cond-mat/0103571* (2001).
- ⁵⁰ I. D. R. Mackinnon, P. C. Talbot, and J. A. Alarco, Phonon Dispersion Anomalies and Superconductivity in Metal Substituted MgB_2 , *Computational Materials Science* 130, 191 (2017).
- ⁵¹ A. Y. Liu, I. I. Mazin, and J. Kortus, Beyond Eliashberg Superconductivity in MgB_2 : Anharmonicity, Two-Phonon Scattering, and Multiple Gaps, *Physical Review Letters* 87, 087005 (2001).
- ⁵² H. Rosner, W. E. Pickett, S.-L. Drechsler, A. Handstein, G. Behr, G. Fuchs, K. Nenkov, K.-H. Müller, and H. Eschrig, Electronic Structure and Weak Electron-Phonon Coupling in TaB_2 , *Phys. Rev. B* 64, 144516 (2001).
- ⁵³ Z. Yu, T. Bo, B. Liu, Z. Fu, H. Wang, S. Xu, T. Xia, S. Li, S. Meng, and M. Liu, Superconductive Materials with MgB_2 -like Structures from Data-Driven Screening, *Phys. Rev. B* 105, 214517 (2022).
- ⁵⁴ D. E. Sands, C. F. Cline, A. Zalkin, and C. L. Hoenig, The Beryllium-Boron System, *Acta Cryst* 14, 309 (1961).
- ⁵⁵ J. E. Moussa, J. Noffsinger, and M. L. Cohen, Possible Thermodynamic Stability and Superconductivity of Antifluorite $\text{Be}_2\text{B}_x\text{C}_{1-x}$, *Phys. Rev. B* 90, 064109 (2014).
- ⁵⁶ R. N. Shelton, Superconductivity and Crystal Structure of a New Class of Ternary Platinum Borides, *Journal of the Less Common Metals* 62, 191 (1978).
- ⁵⁷ H. C. Ku and G. P. Meisner, Crystal Structure and Physical Properties of New Ternary Rare Earth Borides, *Journal of the Less Common Metals* 78, 99 (1981).
- ⁵⁸ W. Jung, $\text{AnRh}_3\text{n-1B}_2\text{n}$ Mit $\text{A} \equiv \text{Ca}$ Und Sr , Eine Homologe Reihe Ternärer Erdalkali-Rhodiumboride Aus Bauelementen Der CeCo_3B_2 -Und Der CaRh_2B_2 -Struktur, *Journal of the Less Common Metals* 97, 253 (1984).
- ⁵⁹ A. S. Sobolev, Yu. B. Kuz'ma, T. E. Soboleva, and T. F. Fedorov, Phase Equilibria in Tantalum — Titanium — Boron and Tantalum — Molybdenum — Boron Systems, *Powder Metall Met Ceram* 7, 48 (1968).
- ⁶⁰ Yu. B. Kuz'ma, An X-Ray Structural Investigation of the Systems Niobium-Titanium-Boron and Niobium-Molybdenum-Boron, *Powder Metall Met Ceram* 10, 298 (1971).
- ⁶¹ W. Jung, Ternäre Seltenerd-Iridiumboride SEIr_2B_2 ($\text{SE} \equiv \text{Y, La, Ce, Pr, Nd, Sm, Eu, Gd, Tb, Dy}$) Mit CaRh_2B_2 -Struktur, *Journal of the Less Common Metals* 171, 119 (1991).
- ⁶² E. V. Sampathkumaran and I. Das, Magnetic Behavior of CeIr_2B_2 , *Phys. Rev. B* 51, 8628 (1995).
- ⁶³ N. B. Bolotina, O. N. Khrykina, A. N. Azarevich, N. Yu. Shitsevalova, V. B. Filipov, S. Yu. Gavrilkin, K. V. Mitsen, V. V. Voronov, and N. E. Sluchanko, Checkerboard Patterns of Charge Stripes in the Two-Gap Superconductor ZrB , *Phys. Rev. B* 105, 054511 (2022).
- ⁶⁴ T. Sun, D.-B. Zhang, and R. M. Wentzcovitch, Dynamic Stabilization of Cubic Ca Si O_3 Perovskite at High Temperatures and Pressures from Ab Initio Molecular Dynamics, *Phys. Rev. B* 89, 094109 (2014).
- ⁶⁵ Y.-N. Wu, W. A. Saidi, J. K. Wuenschell, T. Tadano, P. Ohodnicki, B. Chorpene, and Y. Duan, Anharmonicity Explains Temperature Renormalization Effects of the

- Band Gap in SrTiO₃, *J. Phys. Chem. Lett.* 11, 2518 (2020).
- ⁶⁶ T. Yue, Y. Zhao, J. Ni, S. Meng, and Z. Dai, Strong Quartic Anharmonicity, Ultralow Thermal Conductivity, High Band Degeneracy and Good Thermoelectric Performance in Na₂TlSb, *Npj Comput Mater* 9, 17 (2023).
- ⁶⁷ K. Shirai, K. Sakuma, and N. Uemura, Theoretical Study of the Structure of Boron Carbide B₁₃C₂, *Phys. Rev. B* 90, 064109 (2014).
- ⁶⁸ Y. Katsura, A. Yamamoto, H. Ogino, S. Horii, J. Shimoyama, K. Kishio, and H. Takagi, On the Possibility of MgB₂-like Superconductivity in Potassium Hexaboride, *Physica C: Superconductivity and Its Applications* 470, S633 (2010).
- ⁶⁹ I. R. Shein and A. L. Ivanovskii, Superconductivity in Be₂B? Comparative Analysis of the Band Structure of MgB₂, BeB₂ and Be₂B, *Phys. Stat. Sol. (b)* 227, R1 (2001).
- ⁷⁰ L. A. J. Garvie, H. Hubert, W. T. Petuskey, P. F. McMillan, and P. R. Buseck, High-Pressure, High-Temperature Syntheses in the B–C–N–O System, *Journal of Solid State Chemistry* 133, 365 (1997).
- ⁷¹ H. J. Choi, D. Roundy, H. Sun, M. L. Cohen, and S. G. Louie, The Origin of the Anomalous Superconducting Properties of MgB₂, *Nature* 418, 6899 (2002).